

# Numerical investigation of aerodynamic and acoustic characteristics of bionic airfoils inspired by bird wing

Proc IMechE Part G:  
*J Aerospace Engineering*  
0(0) 1–13  
© IMechE 2018  
Article reuse guidelines:  
sagepub.com/journals-permissions  
DOI: 10.1177/0954410018812617  
journals.sagepub.com/home/pig



Menghao Wang and Xiaomin Liu

## Abstract

Airfoil is the basic element of fluid machinery and aircraft, and the noise generated from that is an important research aspect. Aiming to reduce the aerodynamic noise around the airfoil, this study proposes an airfoil inspired by the long-eared owl wing and another airfoil coupled with the bionic airfoil profile, leading edge waves, and trailing edge serrations. Numerical simulations dependent on the large eddy simulation method coupled with the wall-adapting local eddy-viscosity model and the Ffowcs Williams and Hawkings equation are conducted to compare the aerodynamic and acoustic characteristics of two types of bionic airfoils at low Reynolds number condition. The simulations reveal the dipole characteristic of acoustic source and sound pressure level distribution at various frequencies. Two types of bionic airfoils show lower noise compared with the conventional NACA 0012 airfoil with a similar relative thickness of 12%. Compared with the bionic airfoil, the average value of sound pressure level at the monitoring points around the bionic coupling airfoil is decreased by 9.94 dB, meanwhile the lift-to-drag ratio also keep higher. The bionic coupling airfoil exerts a suppression of sound pressure fluctuation on the airfoil surfaces, which result from that the range and size of separation vortices are reduced and the distance between vortices and airfoil surface are increased. The tube-shaped vortices in the wake of airfoil are effectively restrained and split into small scale vortices, which are important to cause less aerodynamic noise around the bionic coupling airfoil. Consequently, a novel bionic coupling airfoil is developed with the excellent aerodynamic and acoustic performance.

## Keywords

Bionic airfoil, bird wing, numerical simulation, aerodynamic performance, noise reduction

Date received: 29 July 2018; accepted: 19 October 2018

## Introduction

Research on the aerodynamic performance of fluid machinery and aircraft, such as fans, wind turbines, and micro/unmanned air vehicles, has continued for a long time. The aerodynamic noise, commonly heard from these practical applications, has also been an important research topic.<sup>1</sup> The airfoil is not only the basic element of blade, but also the main subject of the theoretical and technical research of noise reduction. Therefore, the study of flow noise around airfoil is of typical significance. The traditional active and passive noise reduction measures have made important progresses, but they are still limited by the deterioration of the aerodynamic performance and application condition. Bionic design method has recently made extraordinary progresses as it inherits and develops the distinctive structures of organisms to make an effective solution for noise reduction.

During the long-term evolution and adaptation process in nature, the avian have formed a unique

noise reduction system. Inspired by the efficient flight and low-noise characteristics of the owl, a considerable amount of studies have then been performed to study and utilize the noise reduction behavior of bionic structures. Graham<sup>2</sup> was the first put forward that the owl flew almost slowly and silently in comparison to other birds. Liu et al.<sup>3</sup> adopted the measuring technology for obtaining the airfoil profile distribution of four kinds of bird wings, including the seagull, merganser, teal, and owl, which provided a theoretical reference for the research of aerodynamic and acoustic performance of bird wing models. According to the method provided in Liu

---

School of Energy and Power Engineering, Xi'an Jiaotong University, Xi'an, PR China

### Corresponding author:

Xiaomin Liu, School of Energy and Power Engineering, Xi'an Jiaotong University, 28 West Xianning Road, Xi'an, Shaanxi, Xi'an 710049, PR China.

Email: liuxm@xjtu.edu.cn

et al.,<sup>3</sup> Li et al.<sup>4</sup> reconstructed four kinds of bionic airfoils. The results on the unsteady flow and noise simulations indicated that the seagull airfoil showed the greatest lift-to-drag ( $L/D$ ) ratio among the four kinds of bird wings, and the owl airfoil possessed the excellent noise reduction characteristic. Ge et al.<sup>5</sup> built an owl-wing airfoil based on a silent-flight long-eared owl and studied the flow structures around the owl wing and related sound source. It suggested that the noise was mainly concentrated in the mid frequency and the scattering noise was dominant in noise generation.

Apart from the previous research work, a series of studies have addressed the noise reduction of the airfoil based on the special structures. There were some investigation confirm the bionic structures, especially the leading-edge or trailing-edge waves and serrations, showed a great performance related to noise reduction. Lilley et al.<sup>6</sup> found that the comb-like leading edge and fringe-like trailing edge had a certain function of reducing noise, and pointed out that the three unique forms of the owl could focus on reducing the noise in the frequency band above 2 kHz. Howe<sup>7</sup> was the first to propose the concept of noise reduction by applying a serrated trailing edge design. The serrated structure was found to decide the effectiveness of noise reduction directly. Chong et al.<sup>8,9</sup> confirmed that the serrated trailing edge brought unique result on suppressing tonal instability. As the serrations grew wider, the effect was more significant. Moreau et al.<sup>10</sup> analyzed the noise variation of two kinds of trailing edge serrations adopting experimental method at low Reynolds number ( $Re$ ) condition. It was seen that wider trailing edge serrations could weaken the behavior of turbulent fluctuating velocity, and accordingly decreased the overall sound pressure level (OASPL) by up to 11 dB. In contrast, the OASPL of narrower trailing edge serrations was increased by up to 4 dB. Arina et al.<sup>11</sup> compared NACA 65-1210 airfoil and that airfoil with trailing-edge serrations based on numerical simulation and experiment. The results pointed out that the flow configuration was greatly affected because of the existence of the serrated structures. The power spectral density (PSD) spectra showed that the airfoil with serrations exerted a lower PSD in the low- and mid-frequency sections. Ito<sup>12</sup> studied the effect of the leading edge serrations on the aerodynamic and acoustic characteristics at low Reynolds number condition. The author came to a conclusion that the serrations provided an effective way to suppress the noise and enhanced the lift force at larger angle of attack (AoA). Narayanan et al.<sup>13</sup> experimentally investigated the effect of leading edge serrations on reducing the broadband noise. The study revealed that the serration amplitude was a major factor in noise performance. The sound radiated along the leading edge was effectively interfered that was a root cause for noise reduction. Clair et al.<sup>14</sup> assessed the acoustic performance of the sinusoidal serrations by experimental and

numerical investigations. The work showed that the sinusoidal serrations had great effect on noise reduction without weakening the aerodynamic performance. Ren et al.<sup>15</sup> experimentally revealed the unsmooth leading edge of long-eared owl wing had major implications for its silent flight. Based on the experimental research, the author rebuilt bionic airfoil model coupled with wavy leading edge. The numerical simulation showed that the wavy leading edge of airfoil could delay the boundary layer separation, reduce the airfoil's pressure fluctuation, and turbulence separation. The end results of these appeared obvious reduction of airflow noise and increase of lift force.

The unique bionic structures, such as the airfoil profile, serrated leading edge, and trailing edge, show significant effect on the generation of lower noise. However, the mechanisms of the noise generation and reduction are not yet clearly revealed and further investigations are still needed. Moreover, the above studies are merely based on a unit of bionic structures, which do not really couple with the airfoil profile, leading edge, and trailing edge structures together, therefore greatly restrict the innovative design of the multi-factor bionic coupling airfoil. In this study, we propose an airfoil based on 40% cross-section profile of long-eared owl wing named bionic airfoil, and another airfoil coupled on bionic configurations with the bionic airfoil profile, leading edge waves and trailing edge serrations, which is named as bionic coupling airfoil. In order to analyze the flow fields and their corresponding sound fields of two types of bionic airfoils, the large eddy simulation (LES) method coupled with the wall-adapting local eddy-viscosity (WALE) subgrid-scale model and the Ffowcs Williams and Hawkings (FW-H) equation based on the Lighthill's acoustic analogy are conducted numerically. The study presents here results and mechanisms of noise reduction based on the bionic design technology that will offer beneficial references in the blade design of fluid machineries and air vehicles with lower noise.

## Reconstruction of bionic model

### Extraction of bionic airfoil

Based on the studies of Liu and Liao,<sup>3,16</sup> which are related to the measurement and reconstruction of the long-eared owl wing, the airfoil in the 40% spanwise position of the wing model can be extracted. The airfoil profile is described by adding and subtracting operation between the camber line and thickness distribution, shown as

$$z_u = z_c + z_t \quad (1)$$

$$z_l = z_c - z_t \quad (2)$$

where  $z_u$  and  $z_l$  are the distribution of the upper and lower surfaces profiles, respectively.  $z_c$  and  $z_t$  are the

distribution of the camber line and thickness respectively, defined as

$$\frac{z_c}{c} = \frac{z_{c(\max)}}{c} \eta (1 - \eta) \sum_{n=1}^3 S_n (2\eta - 1)^{n-1} \quad (3)$$

$$\frac{z_t}{c} = \frac{z_{t(\max)}}{c} \sum_{n=1}^4 A_n (\eta^{n+1} - \sqrt{\eta}) \quad (4)$$

where  $c$  is the local chord length,  $x$  is the chordwise coordinate, and  $\eta = x/c$  is the normalized chordwise coordinate.  $z_{c(\max)}$  is the maximum camber line coordinate,  $z_{t(\max)}$  is the maximum thickness coordinate,  $z_{c(\max)}$  and  $z_{t(\max)}$  are expressed as equations (5) and (6).  $S_n$  and  $A_n$  are the coefficients, which can be obtained based on the least-squares method. As a result, the coefficients are given as:  $S_1 = 3.9362$ ,  $S_2 = -0.7705$ ,  $S_3 = 0.8485$ ,  $A_1 = -29.4861$ ,  $A_2 = 66.4565$ ,  $A_3 = -59.8060$ ,  $A_4 = 19.0439$ .

$$\frac{z_{c(\max)}}{c} = \frac{0.18}{1 + 7.31\xi^{2.77}} \quad (5)$$

$$\frac{z_{t(\max)}}{c} = \frac{0.1}{1 + 14.86\xi^{3.52}} \quad (6)$$

where  $\xi$  is the spanwise location.

The airfoil in the 40% spanwise position of the long-eared owl wing performs well on aerodynamics and noise reduction.<sup>16</sup> Consequently, the spanwise location  $\xi$  is selected as 0.4. The airfoil in the 40% spanwise position of the long-eared owl wing is extracted by utilizing the above equations. Figure 1 shows the extracted bionic airfoil profile.

As shown Figure 1, the upper surface of the owl airfoil appears as a large camber, and the lower surface of the owl airfoil is concave, especially at the midstream of airfoil. The parameters, which present the main characteristics of the bionic airfoil, are displayed in Table 1.

### Reconstruction of bionic coupling airfoil

In addition to unique airfoil profile, the unsmooth structures of the owl wing also play a significant part in the noise suppression in a flight. According to Liu,<sup>17</sup> the length and width of owl wing are

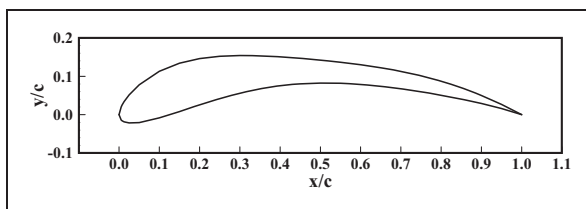


Figure 1. Bionic airfoil profile.

about 400 mm and 200 mm, respectively. The leading edge of owl wing can be regarded as a wavy structure, which can be described by wavelength,  $\lambda = 25\text{--}100\text{ mm}$ , and amplitude,  $a = 5\text{--}20\text{ mm}$ . The trailing edge of the wing can be considered as a serrated structure, which can be described by the serration height,  $h = 10\text{--}18\text{ mm}$ , serration width,  $w = 7\text{--}15\text{ mm}$ , and serration spacing,  $s = 10\text{--}20\text{ mm}$ .

The airfoil in the 40% spanwise position of the owl wing is employed as a benchmark to reconstruct the bionic coupling airfoil. As for the selected airfoil, the length of chord is 100 mm, the camber line is 103.63 mm, and the span length is given as 200 mm. The principle of geometrical similarity is applied to determine that the area ratio of the wing model and airfoil model is  $R_a = A_w/A_b \approx 3.86$  with the length ratio  $R_l = \sqrt{R_a} = 1.96$ . Therefore, the design parameters of the leading edge wave and trailing edge serration of the bionic coupling airfoil can be described and determined, which are shown in Figure 2 and Table 2. In Figure 2, the observed cross-sections of the airfoil, such as S1 and S2 surfaces marked respectively, located at the root and tip of serration, which are corresponding to the peak and root of the wave structure, are selected as concerned study subjects. Finally, the bionic airfoil and the bionic coupling airfoil are constructed, shown in Figure 3.

### Computational methods

The numerical calculation is realized in the following parts. The first part is the calculation of the steady flow field, which is carried out by using the Spalart–Allmaras

Table 1. The main parameters of the bionic airfoil.

Description	Value
Maximum thickness	12.59%
Location of maximum thickness	0.15
Maximum camber	11.36%
Location of maximum camber	0.45

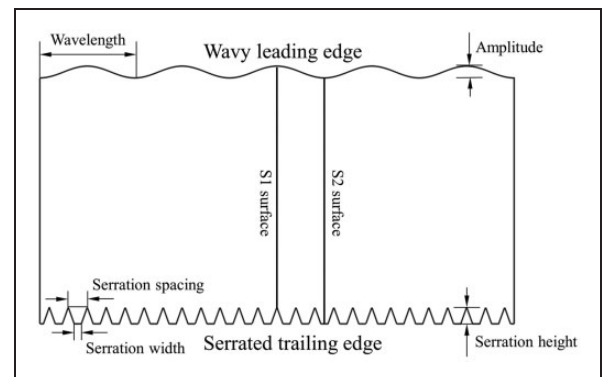
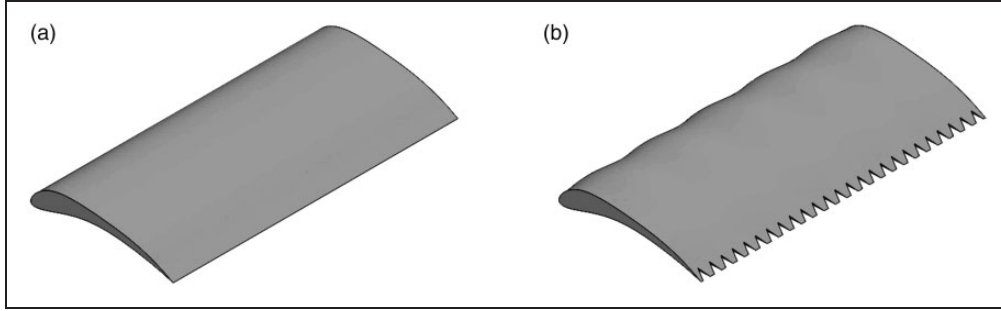


Figure 2. Designed parameters of bionic coupling airfoil.

**Table 2.** Geometrical parameters of the wing and bionic coupling airfoil.

Type	Area, $A$ (mm <sup>2</sup> )	Wavelength, $\lambda$ (mm)	Amplitude, $a$ (mm)	Serration height, $h$ (mm)	Serration width, $w$ (mm)	Serration spacing, $s$ (mm)
Wing model	400 × 200	25–100	5–20	10–18	7–15	10–20
Bionic coupling airfoil	200 × 103.63	12.72–50.90	2.54–10.18	5.09–9.16	3.56–7.63	5.09–10.18
Selected values	200 × 103.63	40	5	7	5	8

**Figure 3.** Geometrical models of two types of bionic airfoils: (a) bionic airfoil; and (b) bionic coupling airfoil.

(S-A) turbulence model. The purpose of the second step is to calculate the unsteady flow field, which is solved by adopting the LES method coupled with the WALE model based on the steady flow results. In the last part of the simulation, the unsteady flow results are applied as initial condition in the FW-H equation to make a specific prediction about the acoustic behavior of airfoil. The involved equations will be discussed later in this chapter.

The three-dimensional incompressible Navier–Stokes (N-S) equation is solved based on the finite-volume method (FVM). The SIMPLE algorithm based on pressure and velocity coupling is used as the numerical solution method. Green–Gauss cell-based gradient evaluation is applied to calculate the gradients of the variables. For the spatial discretization of the pressure and momentum, the second-order scheme and the second-order upwind scheme are employed respectively. The transient formulation is determined by using the second-order implicit scheme. In the process of unsteady calculation, the time step size ( $\Delta t$ ) is of significance in numerical result, assigned as  $5 \times 10^{-5}$  s to make sure the computational requirement of Courant–Friedrichs–Lewy (CFL) number less than 1. In this work, all numerical simulations are conducted in ANSYS Fluent 18.0 software.

### The LES model

LES turbulence model as an appropriate approach for the calculation of transient flow field is often adopted to carry out the similar problem.<sup>18</sup> The governing equations of the LES can be obtained by filtering the time-dependent N-S equations in configuration

space. The concrete filtering process is described in detail in the following description.

Filtering function  $\bar{\phi}(X, t)$  related to space variable  $\phi$  is defined with the integral form

$$\bar{\phi}(X, t) = \int_D \phi(X', t) G(X - X') dX' \quad (7)$$

where  $D$  is the involved fluid domain and  $G$  is the filter function.

The “top hat filter” operation based on the previous experimental or numerical results is generally expressed as

$$\bar{\phi}(X, t) = \frac{1}{V} \int_v \phi(X', t) dX', \quad X' \in v \quad (8)$$

where  $V$  is the volume of a computational element. The filter function  $G$  is described as

$$G(X) = \begin{cases} 1/V, & X' \in v \\ 0, & X' \notin v \end{cases} \quad (9)$$

Finally, the incompressible N-S equations can be filtered, rewritten as

$$\rho \frac{\partial \bar{u}_i}{\partial x_i} = 0 \quad (10)$$

$$\rho \frac{\partial \bar{u}_i}{\partial t} + \rho \frac{\partial}{\partial x_j} (\bar{u}_i \bar{u}_j) = -\frac{\partial \bar{P}}{\partial x_i} + \mu \nabla^2 \bar{u}_i - \frac{\partial \tau_{ij}}{\partial x_j} \quad (11)$$

where  $\rho$  represents the fluid density, and  $u_i$  represents the component of the fluid velocity in the  $x_i$  direction.  $\tau_{ij} = \rho \bar{u}_i \bar{u}_j - \rho \overline{u_i u_j}$  is the subgrid-scale stresses tensor.

Considering that  $\tau_{ij}$  as an unknown quantity demands to be modeled, the eddy-viscosity assumption is proposed as

$$\tau_{ij} - \frac{1}{3}\tau_{kk}\delta_{ij} = -2\mu_t\bar{S}_{ij} \quad (12)$$

$$\bar{S}_{ij} = \frac{1}{2}\left(\frac{\partial\bar{u}_i}{\partial x_j} + \frac{\partial\bar{u}_j}{\partial x_i}\right) \quad (13)$$

where  $\bar{S}_{ij}$  is the rate-of-strain tensor for the resolved scale and  $\mu_t$  is the subgrid-scale turbulent viscosity. It is found that the WALE model is well suited for complicated flow conditions in several different LES models.<sup>19</sup> Therefore,  $\mu_t$  is given by

$$\mu_t = \rho L_s^2 \frac{(S_{ij}^d S_{ij}^d)^{3/2}}{(\bar{S}_{ij}^d \bar{S}_{ij}^d)^{5/2} + (S_{ij}^d S_{ij}^d)^{5/4}} \quad (14)$$

$$S_{ij}^d = \frac{1}{2}(\bar{g}_{ij}^2 + \bar{g}_{ji}^2) - \frac{1}{3}(\delta_{ij}\bar{g}_{kk}^2) \quad (15)$$

$$\bar{g}_{ij} = \frac{\partial\bar{u}_i}{\partial x_j} \quad (16)$$

$$L_s = \min(k_a d, C_w V^{1/3}) \quad (17)$$

where  $L_s$  is the mixing length for subgrid scales,  $k_a$  is a von Kármán constant,  $d$  is the distance to the closest wall, and  $C_w$  is a constant value of the WALE model, equal to 0.325 by default, which is suitable for numerical calculation in a wide range.

### FW-H equation

The FW-H equation<sup>20,21</sup> as an inhomogeneous wave equation is conducted to carry out the sound field in this paper that can be derived by utilizing the continuity equation and the N-S equations. Therefore, the obtained equation is written as

$$\begin{aligned} \frac{1}{a_0^2} \frac{\partial^2 p'}{\partial t^2} - \nabla^2 p' &= \frac{\partial^2}{\partial x_i \partial x_j} \{T_{ij} H(f)\} \\ &- \frac{\partial}{\partial x_i} \{[P_{ij} n_j + \rho u_i (u_n - v_n)] \delta(f)\} \\ &+ \frac{\partial}{\partial t} \{[\rho_0 v_n + \rho (u_n - v_n)] \delta(f)\} \end{aligned} \quad (18)$$

where  $a_0$  and  $p'$  are the sound speed and the sound pressure at the far field, respectively.  $\rho_0$  is the static density of fluid without acoustic disturbance,  $f$  is a moving Kirchhoff surface,  $u_i$  is the fluid velocity component in the  $x_i$  direction,  $u_n$  is the fluid velocity component normal to the surface  $f=0$ ,  $v_i$  is the surface velocity components in the  $x_i$  direction,  $v_n$  is the surface velocity component normal to the surface,  $n_i$  is the unit

normal vector pointing toward the exterior region.  $\delta(f)$  and  $H(f)$  are Dirac delta function and Heaviside function, respectively.  $P_{ij}$  is the compressive stress tensor.  $T_{ij}$  is the Lighthill stress tensor, expressed as

$$T_{ij} = \rho u_i u_j + P_{ij} - a_0^2 (\rho - \rho_0) \delta_{ij} \quad (19)$$

In equation (18), the first term on the right-hand side is on behalf of quadrupole source generated by the volume source. The second and third terms on the right-hand side on behalf of dipole and monopole source possess surface source characteristics, which are caused by the action of fluid on the airfoil surface and fluid volume change respectively. In this study, the bionic airfoils are considered as rigid bodies, and the flow is deemed low subsonic and incompressible. Thus, the quadrupole and monopole sources make little contribution to sound source, which can be ignored and dropped. The dipole source term represents the contribution of the unsteady force on the solid wall, which is deemed to be the main sound source.

### Calculation domain and boundary conditions

To make the numerical calculation more reasonable and believable, it is essential to build appropriate calculation domain and boundary conditions. The first half of the calculation domain is established as a semi-cylinder model, and the last part of calculation domain is set as a cuboid model. The top of the calculation domain is expanded as 10 times of the chord length ( $c$ ) from the leading edge of the airfoil, while the bottom of the calculation domain is placed  $20c$  from the trailing edge of the airfoil. The spanwise length is chosen as  $2c$  to make sure that it is much greater than the spanwise coherence length.<sup>22</sup> The calculation domain, which is suitable for the numerical simulation on flowing around airfoil, is determined and is represented in Figure 4.

The boundary conditions of calculation domain shown in Figure 4 are set as follows. The front, top, and bottom surfaces of calculation domain are regarded as the velocity-inlet boundary conditions defined as 8 m/s according to the flight velocity of

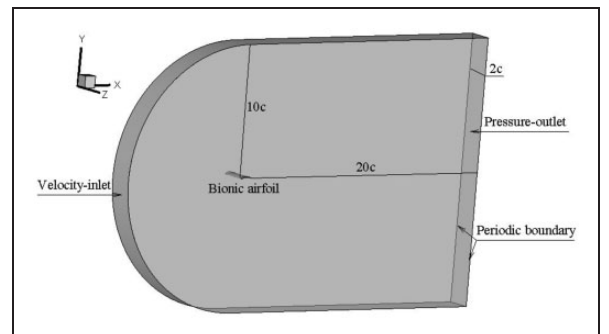


Figure 4. Calculation domain and boundary conditions.



long-eared owl. The Reynolds number of two bionic airfoils based on the chord length is approximately  $5.4 \times 10^4$ , which is close to the operation requirement for most of the fluid machineries and micro/unmanned air vehicles. The pressure-outlet boundary condition is placed at the bottom surface of the calculation domain. In order to minimize the effect of reversed flow, the outlet pressure is given as 101,325 Pa. The two surfaces in the spanwise direction are regarded as periodic boundary conditions. The nonslip condition is employed for the two bionic airfoil surfaces.

### Grid independence and accuracy test

Considering the complexity of the serrations and waves of the bionic coupling airfoil, unstructured grid with great adaptability to complex boundaries is adopted, and the local grids of the airfoil surface are refined. The all grids are generated by ANSYS Mesh software. To meet the calculating requirement of LES model, the first layer grid thickness normal to the airfoil surface is chosen to be close to the value of wall  $y$  plus ( $y^+$ ) less than 1.<sup>23,24</sup> The values of  $y^+$  distributed in the airfoil walls along the span direction are shown in Figure 5. As seen in the figures, it is clear that the maximum values of  $y^+$  are less than 1 for both the airfoils. The grid independence is employed for the determination of appropriate grid number. The verified results are shown in Table 3 by examining

the lift coefficients at  $\text{AoA}=0^\circ$  for five different grid numbers. To save the computational cost and sustain the calculation precision, the grid of  $3.27 \times 10^6$  and  $4.17 \times 10^6$  are adopted respectively as the final grid number for present simulations of the bionic airfoil and the bionic coupling airfoil. At the same time, the numerical grids we adopted also meet the needs of acoustic calculation. Figure 6 shows the local grids near the bionic coupling airfoil.

As for the numerical study, it is an important approach to verify the accuracy of numerical methods. Therefore, the pressure coefficient distribution on the NACA0012 airfoil surface at  $\text{Re}=2.88 \times 10^6$  with  $\text{AoA}=0^\circ$  and  $\text{AoA}=10^\circ$  are plotted and compared with the previous experiment.<sup>25</sup> Figure 7 shows the result of the validation test of the present numerical simulation. Although there are some tiny discrepancies between the present numerical data and the previous experimental data, the numerical results consist well with the experimental results in the reference that confirms the efficiency and accuracy of the numerical method in this paper. The verification of acoustic calculation based on the LES/FW-H method have been studies in the reference papers.<sup>26,27</sup> Figure 8 shows the Courant number distribution of two airfoils. As seen in the figures, there is no doubt that the Courant numbers are less than 1 for both the airfoils. Therefore, the transient calculation achieves the requirement of the CFL condition.

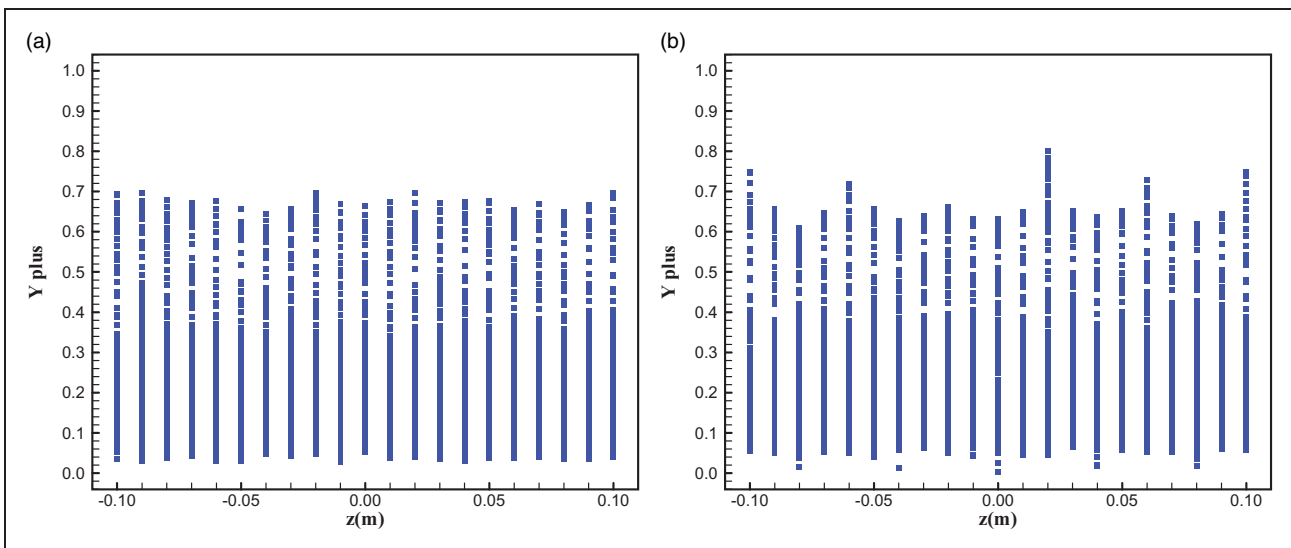
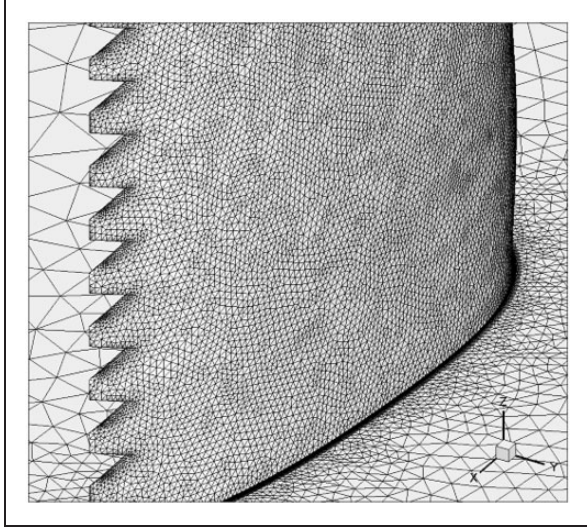


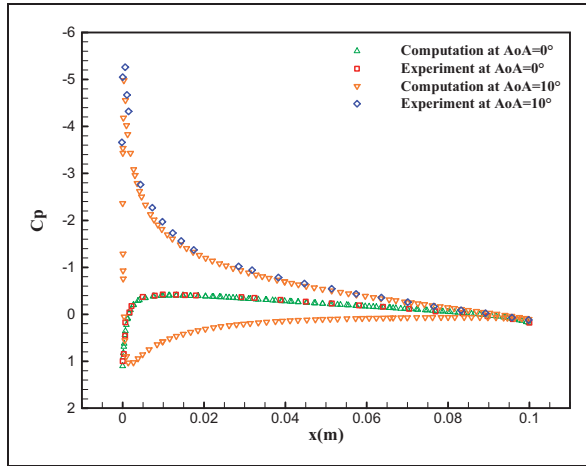
Figure 5.  $y^+$  distribution of the airfoil walls: (a) bionic airfoil; and (b) bionic coupling airfoil.

Table 3. Variation of the grid number on the lift coefficient.

Bionic airfoil	Grid number/ $10^4$	76	162	230	327	450
	Lift coefficient	0.91879	0.82284	0.75830	0.73372	0.73377
Bionic coupling airfoil	Grid number/ $10^4$	135	235	334	417	500
	Lift coefficient	0.91214	0.85857	0.76910	0.74680	0.74700



**Figure 6.** Local grids near the bionic coupling airfoil.



**Figure 7.** Comparison of the present computation and previous experiment.

## Results and discussion

### Aerodynamic performance

Figure 9 shows the comparison of the  $L/D$  ratios for two bionic airfoils. It seems to be more noticeable that the variation on the  $L/D$  ratios of two bionic airfoils presents a same tendency, and the  $L/D$  ratios begin to decrease at the AoA above  $5^\circ$ . It is obvious that the bionic coupling airfoil performs higher  $L/D$  ratios, especially in the range of AoA from  $5^\circ$  to  $25^\circ$ . The bionic coupling airfoil displays the greatest  $L/D$  ratio up to 26.79 at  $\text{AoA} = 5^\circ$ , for comparison the  $L/D$  ratio of the bionic airfoil is lower determined as 25.65. To accord with the practical condition of a centrifugal fan, the AoA of  $16^\circ$  is adopted based on the blade installation angle in this study. There is a distinct difference that the bionic coupling airfoil is still advantageous to generate the greater  $L/D$  ratio at  $\text{AoA} = 16^\circ$  compared with the bionic airfoil. It can

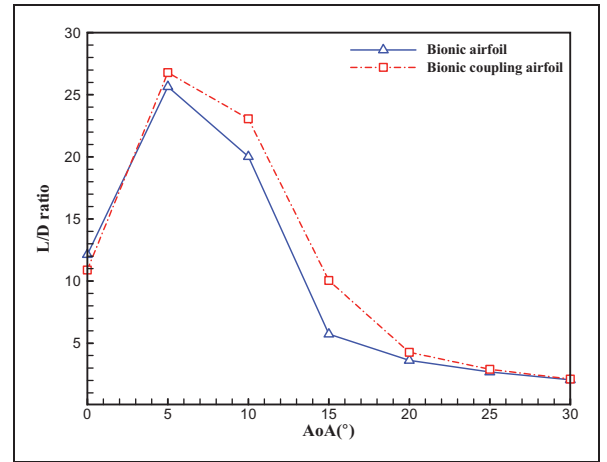


**Figure 9.**  $L/D$  ratios of two bionic airfoils.

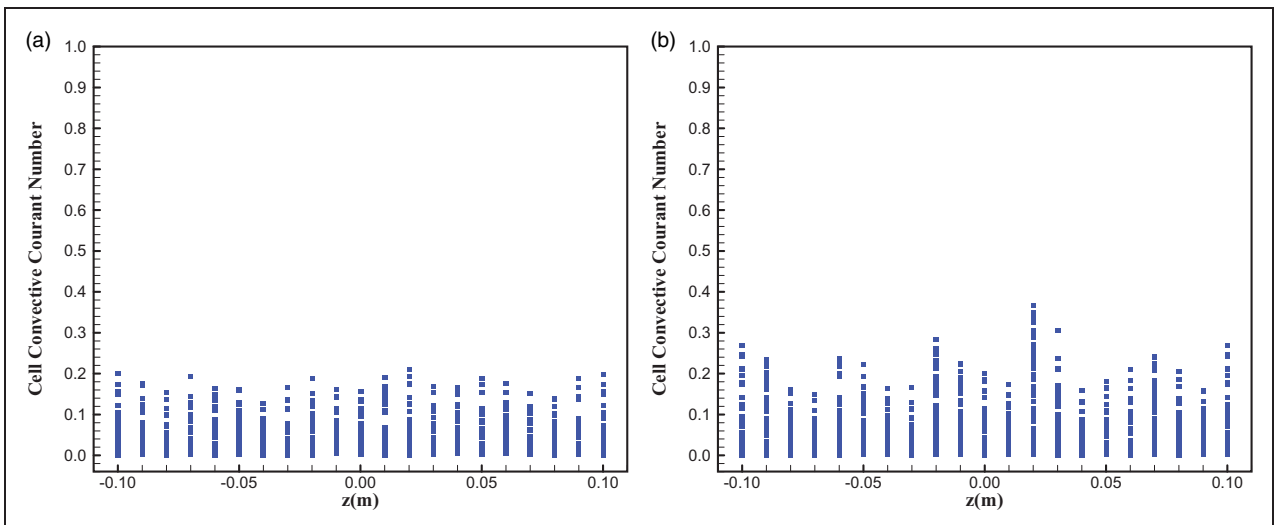


**Figure 8.** Courant number distribution of two airfoils: (a) bionic airfoil; and (b) bionic coupling airfoil.

be concluded that the unsmooth structures including the leading edge waves and trailing edge serrations produce a real effect on emerging high  $L/D$  ratios for the bionic coupling airfoil.

Figure 10 shows the pressure coefficients distribution of S1 surface for the bionic airfoil and S1 and S2 surfaces for the bionic coupling airfoil at  $AoA=16^\circ$ . It can be seen that the two bionic airfoils appear the same pressure coefficients distribution. The significant differences are reflected at the upstream and downstream of the airfoil resulting from the unsmooth bionic structures. The pressure coefficients distributed on the pressure surfaces of two bionic airfoils tend to be gentle behind the location of 0.01 m, and it terminates at the root of the serrations due to the blunt trailing edge of the bionic coupling airfoil in S1 surface. The pressure coefficients distributed on the suction surfaces of both two bionic airfoils show large negative values, especially at 0.008 m form a negative pressure peak which strongly illustrates the suction surface, at the leading edge in particular, makes a greater promotion to the generation of lift force. It can also be found that the positive pressure region becomes wider in the suction surface of the bionic coupling airfoil because of the protrusion of leading edge. After the pressure peak in the suction surface, the airfoils experience a negative pressure gradient with a similarity of trend. It concludes that the bionic coupling airfoil shows the better aerodynamic performance by analyzing the results of the  $L/D$  ratio and pressure coefficients distribution of two bionic airfoils.

### Acoustic characteristics

In order to reveal the sound source propagation direction, the directivity characteristics of sound pressure level (SPL) of two bionic airfoils are shown in Figure 11, and the conventional NACA0012 airfoil is adopted as a contrastive airfoil which possesses a

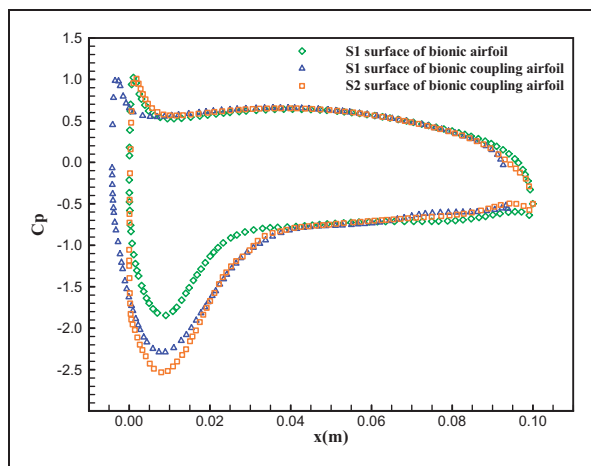


**Figure 10.** Pressure coefficients distribution on two bionic airfoil surfaces.

relative thickness of 12% alike with that of two bionic airfoils. The distance from the noise monitoring points to the center of the airfoil chord are  $10c$  with increment of  $30^\circ$  for the angle of the monitoring points. In particular, the radiation angle of  $0^\circ$  corresponds to the direction of the free-stream and the direction of  $90^\circ$  is vertically located above the airfoil. It can be seen that the SPL of two airfoils varies with the radiation angle. The noise radiation behavior reveals that the sound source tends to radiate to upward and downward sides, which reasonably concludes that the dipole source is dominant in the process of sound propagation. It is interesting to note that the directivity of SPL of the bionic coupling airfoil rotates counterclockwise slightly. This phenomenon may relate to the trailing edge serrations, which provide flow channels for the airflow from the pressure surface to the suction surface and thus form a flow in a counterclockwise direction. Another reason is that the streamwise turbulence intensity presents a certain coherence effect in the opposite direction of incoming flow, which is related to the noise propagation. Compared with the noise generated by the NACA0012 airfoil, the noise of two bionic airfoils is decreased significantly, particularly in the upward side and downward side of noise radiation. The numerical results show that the average SPL at the 12 monitoring points of the NACA0012 airfoil, bionic airfoil and bionic coupling airfoil is 45.24, 42.64, and 32.70 dB, respectively.

The noise spectra indicate the variations of the SPL in different frequency ranges. Figure 12 shows the SPL spectra of the NACA0012 airfoil and two

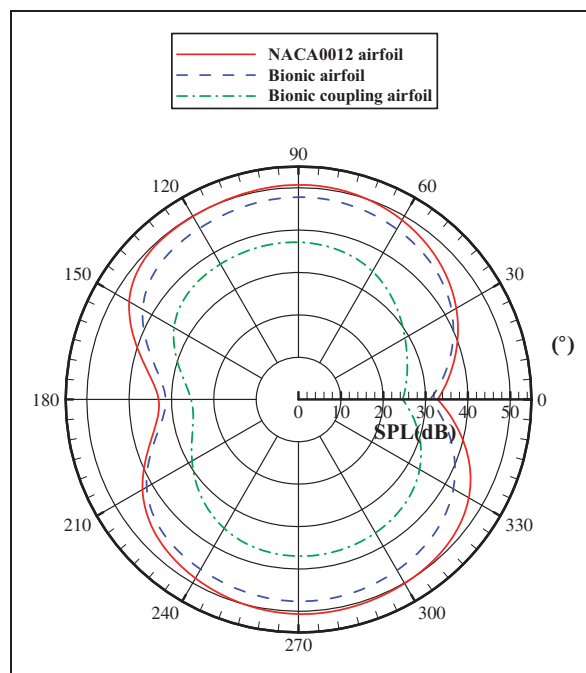


**Figure 11.** Directivity characteristics of sound pressure level (SPL).



bionic airfoils at the noise receiving point (the direction of  $90^\circ$ ) where the airfoils generate the maximum value of noise. As shown in Figure 12, it is clear that the noise variation tendency of three airfoils is basically the same and the noise is mainly generated in the low-frequency section. Therefore, it is concluded that

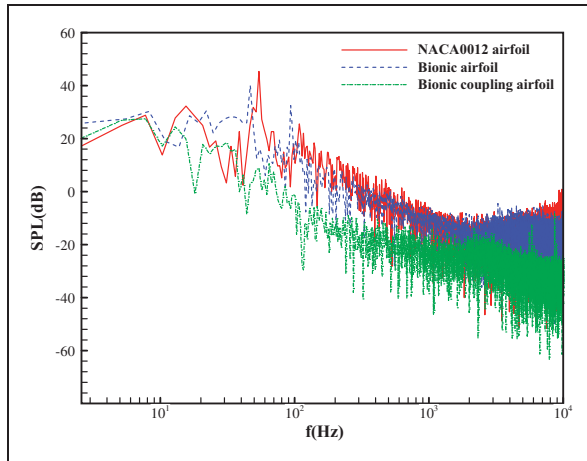


**Figure 12.** SPL spectra of the NACA0012 airfoil and two bionic airfoils.

the low-frequency noise introduced by flowing over the airfoil plays an important part in the overall noise at a relatively low Reynolds number. It is obvious that there is no obvious peak value in the SPL spectra of the bionic coupling airfoil. It also can be seen that the bionic coupling airfoil generates lower noise than other two airfoils at the frequency from 0 to 10,000 Hz. Combined with the analysis of directivity characteristics of the SPL, the bionic coupling airfoil presents an obvious advantage in the control of aerodynamic noise.

### Mechanism of noise reduction

Figure 13 shows the contours of pressure with streamlines in S1 and S2 surfaces of two airfoils for the purpose of analyzing the instantaneous flow fields clearly. It is demonstrated that a high-pressure area emerges at the leading edge of two bionic airfoils because of the impact of incoming flow. The flow attachment occurs on the pressure surface when the airflow encounters the airfoil, while the flow over the suction surface begins to separate. A negative pressure center located in the wake of the bionic airfoil is formed because of the effect of the fluid viscosity and flow separation. Under a function of the pressure gradient,

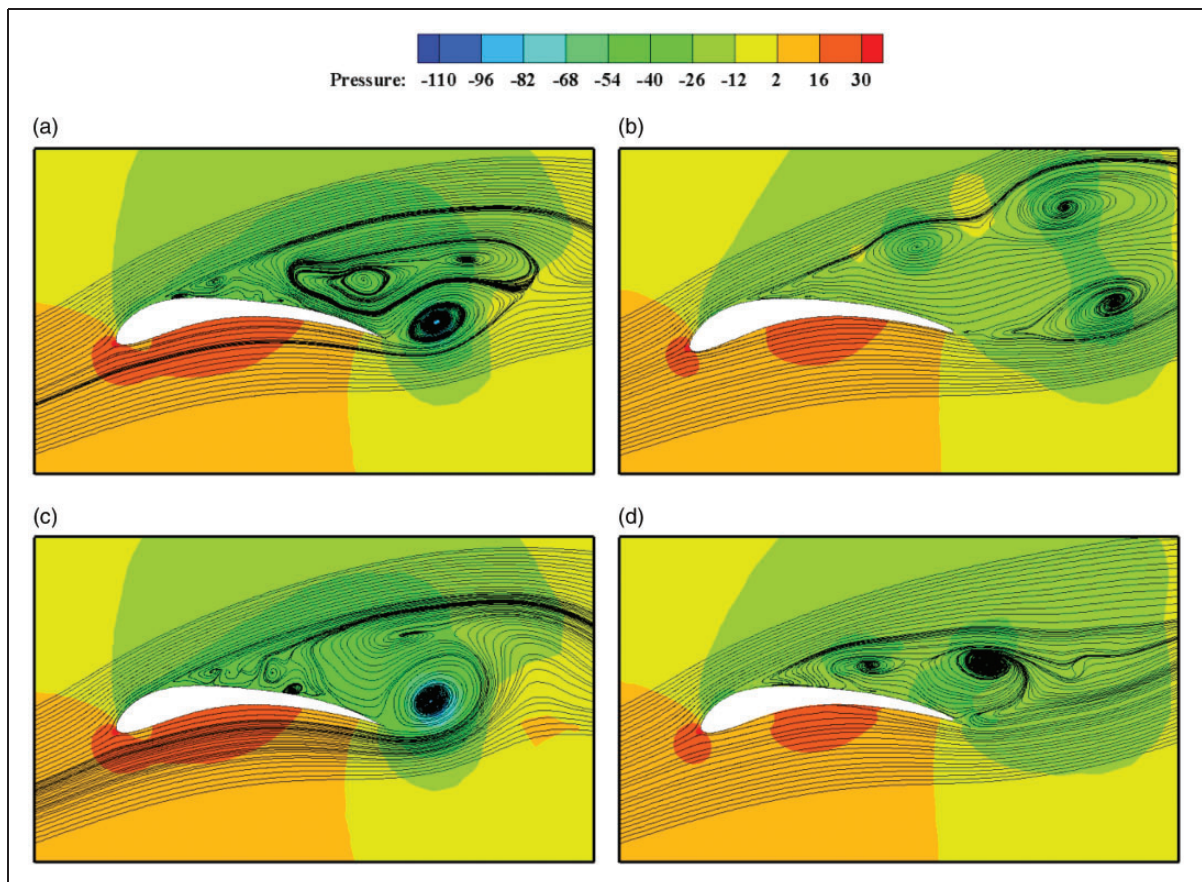


**Figure 13.** Contours of pressure with streamlines: (a) S1 surface of bionic airfoil; (b) S1 surface of bionic coupling airfoil; (c) S2 surface of bionic airfoil; and (d) S2 surface of bionic coupling airfoil.

the downstream flow rolls up to form a large vortex in the trailing edge and several vortices in the upper surface of bionic airfoil. These vortices gradually mix with the main stream and eventually shed. Compared with the bionic airfoil, the trailing edge serrations of the bionic coupling airfoil provide flow channels for the airflow from the pressure surface to the suction surface that may change the location of the vortices. Thus, in S1 and S2 surfaces of bionic coupling airfoil, it can be seen that the distance between the corresponding vortices centers and airfoil surface are increased markedly along with the range and size of the vortices reduced significantly.

The turbulence intensity is utilized to analyze the time-average characteristics of the flow around the airfoils.<sup>28</sup> The streamwise and normal turbulence intensities are defined as

$$T_u = \frac{1}{U_o} RMSu' \quad (20)$$

$$T_v = \frac{1}{U_o} RMSv' \quad (21)$$

where  $u'$  and  $v'$  are the root mean square (RMS) of the turbulence velocities in the streamwise

and normal directions, respectively.  $U_o$  is the incoming velocity.

The turbulence intensity distribution in S1 and S2 surfaces is similar, so the contours of streamwise and normal turbulence intensities in S1 surface are given, shown in Figure 14. The streamwise turbulence intensity is mainly distributed in the suction surfaces of two airfoils. There is a strong turbulence area in the region of the downstream of the bionic airfoil by the action of wake vortices. The turbulence occurs in the mid-stream of the suction surface of the bionic coupling airfoil and prevails in the further downstream region. Analyzing the normal turbulence intensity, it can be seen that the generation of high turbulence intensity is exhibited in the wake region of the bionic airfoil, which may result from the interaction of the airflow from the pressure surface and the suction surface, and subsequent high turbulence pulsation with reversed gradient. In contrast, the highly turbulent region stays away from the bionic coupling airfoil surface, and the turbulence intensity obviously gets weakened, which are important to cause less aerodynamic noise.

The iso-surface of the second invariant  $Q^{29,30}$  as a superior approach for visualizing instantaneous flow structures is adopted to analyze the effect of

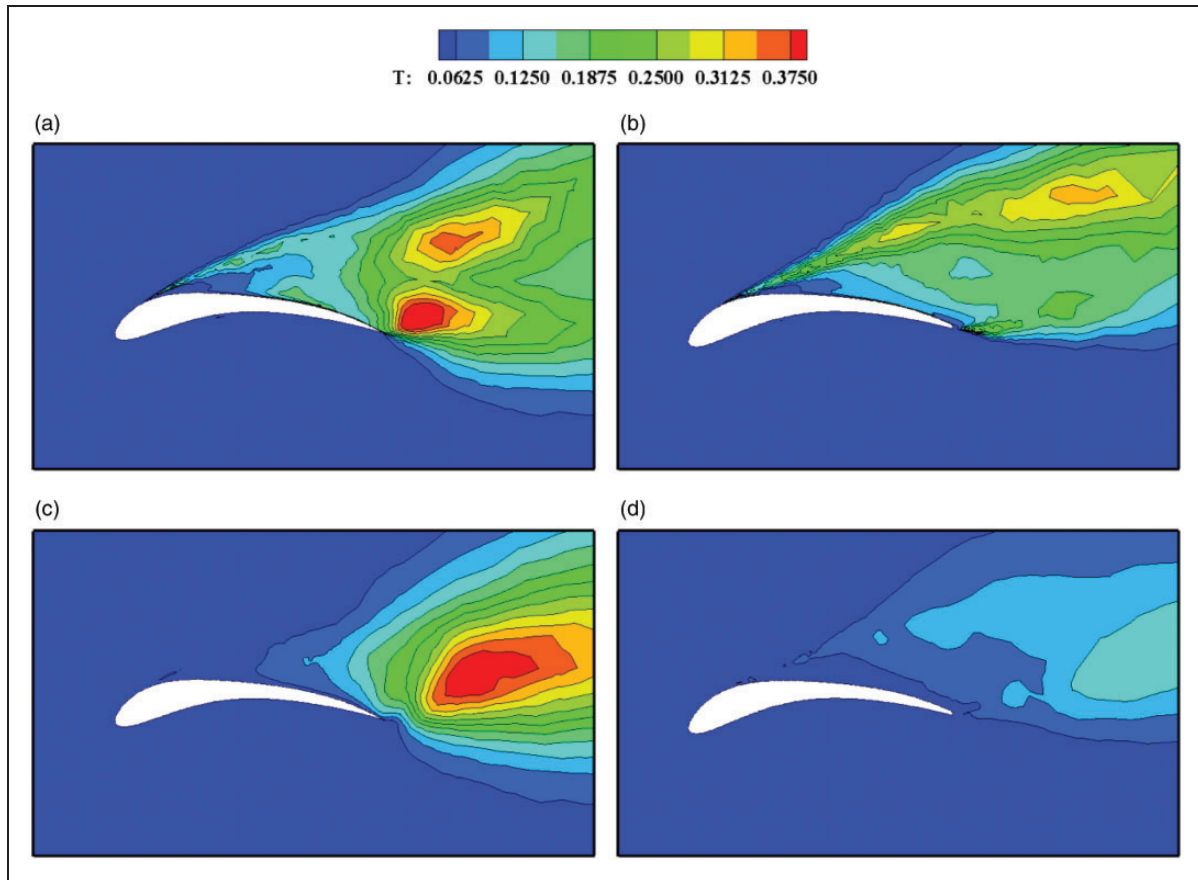


**Figure 14.** Contours of turbulence intensity in S1 surface: (a) streamwise turbulence intensity around bionic airfoil; (b) streamwise turbulence intensity around bionic coupling airfoil; (c) normal turbulence intensity around bionic airfoil; and (d) normal turbulence intensity around bionic coupling airfoil.

three-dimensional vortex structures on noise generation. Figure 15 displays the instantaneous  $Q$  iso-surfaces of the fluid vorticity in the near-wall domain. For both the bionic airfoils, the visible vortices do not appear on the pressure surfaces, while the lamellar vortices are attached to the upstream of the suction surfaces. The great difference of vortex patterns appear on the midstream and downstream of the airfoil suction surfaces. It appears more clearly that the

trailing edge vortex around the bionic airfoil develops to tube-shaped vortices and evolves into wake vortices, however, the vortex around the bionic coupling airfoil is split into several small scale vortices attached to the trailing edge serrations owing to the presence of the serrated structure, which indicates the beneficial effects on controlling the shedding vortices and wake vortices. As described in the theory of vortex sound,<sup>31</sup> the far-field aerodynamic noise is directly generated

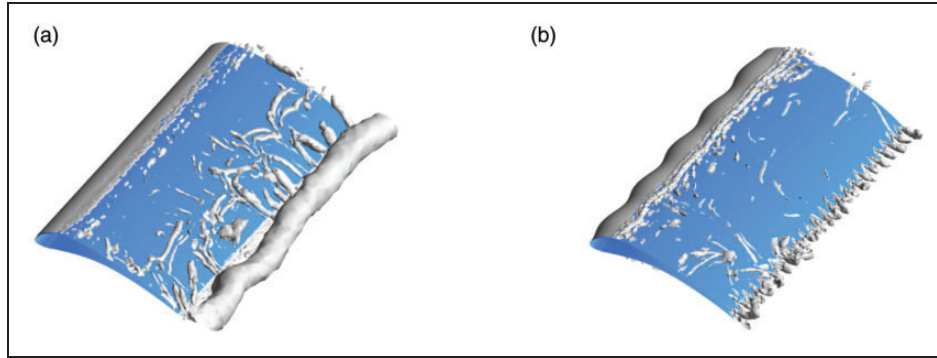


**Figure 15.** Instantaneous  $Q$  iso-surfaces near the two bionic airfoils: (a) bionic airfoil; and (b) bionic coupling airfoil.

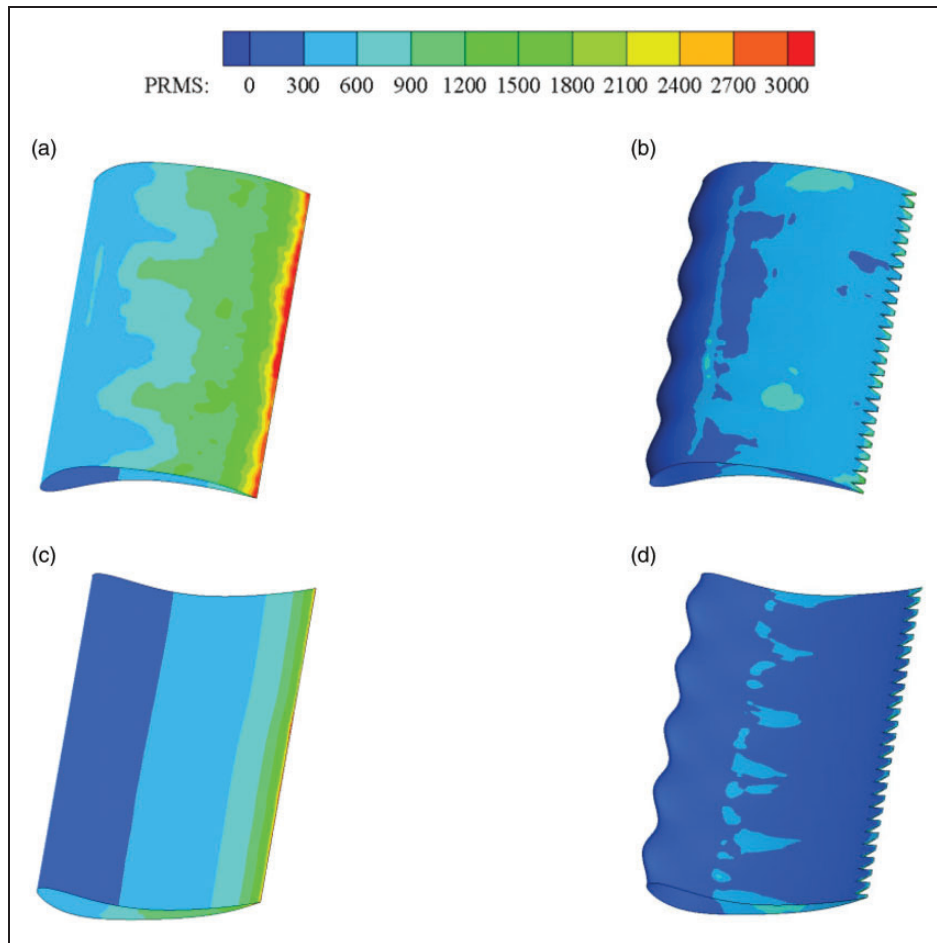


**Figure 16.** PRMS distribution on the surfaces of two bionic airfoils: (a) the suction surface of bionic airfoil; (b) the suction surface of bionic coupling airfoil; (c) the pressure surface of bionic airfoil; and (d) the pressure surface of bionic coupling airfoil.

by the wake vortices and shedding vortices when flowing past the airfoil. Combining with the pressure contours with streamlines and turbulence intensity contours, it is demonstrated that the evolution of the wake vortices and shedding vortices are effectively suppressed by the leading edge waves and trailing edge serrations, thus flow field characteristics of bionic coupling airfoil are superior than that of the bionic airfoil which are closely involved with the generation of aerodynamic noise.

“Surface Dpdt RMS” (PRMS) is defined as the RMS of the time-derivative of static pressure, means the sound pressure fluctuation intensity on the airfoil surface that directly reflects the location and intensity of sound source. Figure 16 shows the distribution of PRMS on the surfaces of two bionic airfoils. For the bionic airfoil, the higher values of PRMS occur in the midstream and downstream of airfoil surface, especially at the trailing edge, and the values located on the pressure surface are lower than that on the suction surface. As for the bionic coupling airfoil, the values of PRMS appear on the suction surface are significantly decreased, and the region with severe sound pressure fluctuation on the pressure surface almost disappears. Coupled with the previous analysis of instantaneous and time-averaged flow field, most of the vortices generated in the downstream of the suction surface cause severe sound pressure pulsation on the same location. The intensity of the sound pressure fluctuation on the bionic coupling airfoil surface can be greatly suppressed. That is the reason why the bionic coupling airfoil reduces unsteady aerodynamic noise when compared with the bionic airfoil.

## Conclusions

Two types of bionic airfoils inspired by bird wing are proposed using the bionic design method in this study. The aerodynamic performance and their corresponding acoustic characteristics around two bionic airfoils are simulated numerically at a relatively low Reynolds number. Some conclusions are achieved as following:

- (1) Both the bionic airfoil and the bionic coupling airfoil possess a high lift-to-drag ratio, and the latter exhibits the greater lift-to-drag ratios, especially in the range of AoA from  $5^\circ$  to  $25^\circ$ . The pressure coefficients distribution of two airfoils at AoA= $16^\circ$  indicates that the upper surface, at the leading edge in particular, makes a greater promotion to the generation of lift force. It seems true that the bionic coupling airfoil shows the better aerodynamic characteristics.
- (2) The acoustic results indicate the dipole source occupies an absolute predominant position in sound field and the noise is mainly generated in the low frequencies. Two types of bionic airfoils show lower noise compared with the conventional NACA 0012 airfoil with a similar relative

thickness of 12%. It has been proven that the bionic coupling airfoil generates lower noise than bionic airfoil, and an average decrease of 9.94 dB is observed at 12 monitoring points.

- (3) The instantaneous and time-average flow fields around the bionic coupling airfoil indicate that the range and size of separation vortices are reduced, as the same time the distance from vortices centers to airfoil surface are increased. There is a strong difference that the tube-shaped vortices in the wake are effectively restrained and split into small scale vortices as for the bionic coupling airfoil. As a result, the bionic coupling airfoil exerts a suppression of sound pressure fluctuation on the airfoil surfaces that is relevant to the generation of noise. It is reasonable to expect that this bionic coupling airfoil will be useful for controlling of aerodynamic noise in the design and application of blade in various industrial machineries.

Some remaining issues including completing optimization of different wavy and serrated parameters for noise reduction performance will be discussed in a later research.

## Declaration of Conflicting Interests

The author(s) declared no potential conflicts of interest with respect to the research, authorship, and/or publication of this article.

## Funding

The author(s) disclosed receipt of the following financial support for the research, authorship, and/or publication of this article: This study was funded by the National Natural Science Foundation of China (No. 51676152) and the Fundamental Research Funds for the Central Universities (No. zrz2017012).

## ORCID iD

Menghao Wang  <http://orcid.org/0000-0001-5956-081X>

## References

1. Mao YJ, Qi DT and Gu YY. Prediction of airfoil noise induced by low-Mach-number flow. *Proc IMechE, Part G: J Aerospace Engineering* 2012; 226: 561–573.
2. Graham RR. The silent flight of owls. *J Roy Aeronaut Soc* 1934; 38: 837–843.
3. Liu TS, Kuykendoll K, Rhew R, et al. Avian wing geometry and kinematics. *AIAA J* 2006; 44: 954–963.
4. Li D and Liu XM. Numerical study on aerodynamic performance and noise characteristic of several bionic airfoils. *J Eng Thermophys* 2015; 36: 2629–2632.
5. Ge CJ, Ge MC, Liang P, et al. Investigation of noise mechanism based on owl wing. *Trans Chinese Soc Agric Mach* 2013; 44: 292–296.
6. Lilley GM. A study of the silent flight of the owl. AIAA Paper 1998-2340, 1998.
7. Howe MS. Aerodynamic noise of a serrated trailing edge. *J Fluids Struct* 1991; 5: 33–45.



8. Chong TP, Joseph P, Vathylakis A, et al. On the noise and wake flow of an airfoil with broken and serrated trailing edges. In: *17th AIAA/CEAS aeroacoustics conference (32nd AIAA aeroacoustics conference)*, Portland, USA, 5–8 June 2011, paper no. 2860.
9. Chong TP and Joseph PF. An experimental study of airfoil instability tonal noise with trailing edge serrations. *J Sound Vib* 2013; 332: 6335–6358.
10. Moreau DJ and Doolan CJ. The generation of tonal noise from sawtooth trailing-edge serrations at low Reynolds numbers. *Aeronaut J* 2016; 120: 971–983.
11. Arina R, Rinaldi RDR, Iob A, et al. Numerical study of self-noise produced by an airfoil with trailing-edge serrations. In: *18th AIAA/CEAS aeroacoustics conference (33rd AIAA aeroacoustics conference)*, Colorado Springs, USA, 4–6 June 2012, paper no. 2184.
12. Ito S. Aerodynamic influence of leading-edge serrations on an airfoil in a low Reynolds number. *J Biomech Sci Eng* 2009; 4: 117–123.
13. Narayanan S, Chaitanya P, Haeri S, et al. Airfoil noise reductions through leading edge serrations. *Phys Fluids* 2015; 27: 025109.
14. Clair V, Polacsek C, Garrec TL, et al. Experimental and numerical investigation of turbulence-airfoil noise reduction using wavy edges. *AIAA J* 2013; 51: 2695–2713.
15. Ren LQ, Sun SM and Xu C. Noise reduction mechanism of non-smooth leading edge of owl wing. *J Jilin Univ* 2008; 38: 128–133.
16. Liao GH. *Aerodynamic, acoustic characteristics of long-eared owl wing and its bionic application*. PhD Thesis, Jilin University, China, 2013.
17. Liu XM, Zhao J and Li D. Noise-reduction mechanism of single-Arc bionic blade with wave shape leading edge coupled with serrated trailing edge. *J Xi'an Jiaotong Univ* 2012; 46: 35–41.
18. Kim HJ, Lee S and Fujisawa N. Computation of unsteady flow and aerodynamic noise of NACA0018 airfoil using large-eddy simulation. *Int J Heat Fluid Flow* 2006; 27: 229–242.
19. Lehmkuhl O, Rodríguez I, Baez A, et al. On the large-eddy simulations for the flow around aerodynamic profiles using unstructured grids. *Comput Fluids* 2013; 84: 176–189.
20. Williams JEF and Hawkings DL. Theory relating to the noise of rotating machinery. *J Sound Vib* 1969; 10: 10–21.
21. Farassat F and Brentner KS. The acoustic analogy and the prediction of the noise of rotating blades. *Theoret Comput Fluid Dyn* 1998; 10: 155–170.
22. Kim HJ, Lee S and Fujisawa N. Computation of unsteady flow and aerodynamic noise of NACA0018 airfoil using large-eddy simulation. *Int J Heat Fluid Flow* 2006; 27: 229–242.
23. Boulkeraa T, Ghenaiet A, Mendez S, et al. A numerical optimization chain combining computational fluid dynamics and surrogate analysis for the aerodynamic design of airfoils. *Proc IMechE, Part G: J Aerospace Engineering* 2014; 228: 1964–1981.
24. Sanei M and Razaghi R. Numerical investigation of three turbulence simulation models for S809 wind turbine airfoil. *Proc I MechE, Part A: J Power & Energy*. Prepublished April 6, 2018; DOI: 10.1177/0957650918767301.
25. Gregory N and O'Reilly CL. Low-speed aerodynamic characteristics of NACA0012 aerofoil section, including the effects of upper surface roughness simulating hoar frost. National Physical Laboratory, NPL Aero Report 1308, USA, 1970.
26. Karthik K, Vishnu M, Vengadesan S, et al. Optimization of bluff bodies for aerodynamic drag and sound reduction using CFD analysis. *J Wind Eng Ind Aerodyn* 2018; 174: 133–140.
27. King WF and Pfizenmaier E. An experimental study of sound generated by flows around cylinders of different cross-section. *J Sound Vib* 2009; 328: 318–337.
28. Nakano T, Fujisawa N, Oguma Y, et al. Experimental study on flow and noise characteristics of NACA0018 airfoil. *J Wind Eng Ind Aerodyn* 2007; 95: 511–531.
29. Hunt JCR, Wray AA and Moin P. Eddies, streams, and convergence zones in turbulent flows. In: *Proceedings of the summer program 1988*, Center for Turbulence Research, 1988, pp.193–208.
30. Lin YF, Lam K, Zou L, et al. Numerical study of flows past airfoils with wavy surfaces. *J Fluids Struct* 2013; 36: 136–148.
31. Powell A. Theory of vortex sound. *J Acoust Soc Am* 1964; 36: 177–195.

## Appendix

### Notation

$c$	chord length of the airfoil
$C_p$	pressure coefficient
$f$	frequency
$L/D$	lift to drag ratio
$Re$	Reynolds number
$T$	turbulence intensity
$T_u$	streamwise turbulence intensity
$T_v$	normal turbulence intensity
$x$	chordwise coordinate
$y$	normalized coordinate
$z$	spanwise coordinate
$\eta$	normalized chordwise coordinate
$\xi$	spanwise location